RSC Advances

PAPER

View Article Online
View Journal | View Issue

Cite this: *RSC Adv.*, 2023, **13**, 35065

Wet chemical synthesis of TGA capped Ag_2S nanoparticles and their use for fluorescence imaging and temperature sensing in living cells†

Mayssa Ibrahim, *[a] P. Camarero,[b] Liyan Ming, [b] Mohamed Haouari,[a] Noura Amamou,[a] P. Haro-González [bc] and Fredj Hassen[d]

In this work, we describe a simple wet chemical route for preparing silver sulfide nanoparticles (Ag_2S) encapsulated with thioglycolic acid (TGA). By using Fourier transform infrared (FTIR) spectroscopy, X-ray diffraction (XRD), energy dispersive X-ray (EDS) microanalysis, transmission electron microscopy (TEM), and dynamic light scattering (DLS), we have found that these nanoparticles were enrobed by TGA molecules and they have an Ag/S ratio nearly equal to 2.2 and a nearly spherical shape with two average size populations. Photoluminescence (PL) spectroscopy has shown that these nanoparticles are highly luminescent, photostable and photobleaching resistant and they emit in the first biologic window with a band peaking in the NIR region at 915 nm. We have demonstrated through a 3-(4,5-dimethyl-thiazol-2yl)-2,5-diphenyltetrazolium bromide (MTT) assay protocol and using U-87 MG human living cells that these nanoparticles are biocompatible with a viability ratio higher than 80% for a concentration equal to 100 μg mL^{-1}. By investigating the effect of pH, ionic strength and thermal quenching on the PL emission, we have shown that these nanoparticles provide a convenient stable tool to measure temperature in the biological range with a relative thermal sensitivity higher than 5% per °C and they may be used as suitable fluorescent probes for living cell imaging and intracellular temperature mapping.

Received 2nd October 2023
Accepted 27th November 2023

DOI: 10.1039/d3ra06705j

rsc.li/rsc-advances

1. Introduction

Materials at the nanometer scale have occurred in nature since the existence of Earth and man has used them for a long time without realizing it.[1] Only in the last few decades have attracted the attention of scientists and they have gained immense interest due to their properties, which are fundamentally different from those of individual atoms or molecules and bulk materials. These physical and chemical properties are due to their small size which results in a large surface to volume ratio and quantum confinement effect of charge carriers in metallic and semiconductor nanostructures.[2]

Due to these unusual characteristics, nanoparticles have found plenty of innovative applications covering different fields such as catalysis, energy production, medicine, agriculture, food industry and so on.[3–6] Accordingly, a new branch of science dealing with the study of the properties of this kind of materials to understand their behaviors has emerged and nanotechnology, which utilizes the knowledge in nanoscience to create new products is sweeping almost every field of science, including physics, materials science, chemistry, biology, computer science, and engineering.[7]

In recent years, it was demonstrated that nanoparticles offer multiple benefits in the diagnosis and treatment of chronic human diseases.[8] Indeed, some nanomaterials are suggested as potential diagnostic noninvasive agent offering high spatial and temporal resolution imaging and thermo-sensing allowing the detection and the visualization on the molecular level, which permit better understanding of the processes that happen in the complex biological systems. Additionally, nanomaterials have advantages that far exceed those of traditional drug carriers since they are nontoxic and biocompatible with higher loading level and they release drugs into the targeted parts of the body, which enhances their effectiveness.[9,10]

However, to better enjoy their benefits for either diagnosis or therapeutic purposes, nanoparticles should have some essential properties including chemical composition, toxicity, physiochemical stability, uniform shape and size distribution, equal amount of functional groups on their surface, convenient pharmacological activity with long blood circulation time whereas they should not generate pathological and physiological undesirable effects. Therefore, these nanoparticles should

[a]*Laboratoire d'Interfaces et de Matériaux Avancés (LIMA), Faculté des Sciences, Université de Monastir, Tunisia. E-mail: mayssabrahim008@gmail.com*

[b]*Nanomaterials for Bioimaging Group, Instituto de Materiales Nicolás Cabrera, Universidad Autónoma de Madrid, Madrid, 2804, Spain*

[c]*Institute for Advanced Research in Chemical Sciences, Universidad Autónoma de Madrid, Madrid, 28049, Spain*

[d]*Laboratoires de Physique des Semi-conducteurs et des Composantes Electroniques (LPSCE), Université de Monastir, Tunisia*

† Electronic supplementary information (ESI) available. See DOI: https://doi.org/10.1039/d3ra06705j

be intensively explored to deeper understand and predict their effects before any use in medical actions.

When dealing with imaging, temperature sensing and thermotherapy, silver sulfide (Ag_2S) nanoparticles are considered as a best choice. This is due to their easy biofunctionalization and very low solubility product constant ($K_{sp} = 6.3 \times 10^{-50}$) which minimizes the release of ions in the biological medium.[11] Moreover, Ag_2S nanoparticles have high absorption coefficient approximately equal to 10^4 m^{-1} and a narrow direct bandgap nearly equal to 1.5 eV with near-infrared (NIR) emission in the transparent biological windows which offers a deep penetration in tissue with minimal photo-damage and low interference with the background auto-fluorescence of the living cells. Additionally, it was recently demonstrated that Ag_2S nanoparticles are highly biocompatible with low cytotoxicity.[12,13] All these characteristics make of these nanoparticles very suitable luminescent nano-probes for sensing and imaging the biological medium at cell scale. Indeed, NIR fluorescent imaging is considered as a suitable solution to overcome the drawbacks of others routinely used imaging techniques such as the use of ionizing radiation which have limited spatial resolution, poor temporal resolution, and complex and expensive instrumentation.[14] Additionally, due to their temperature dependent optical properties, these nanoparticles constitute a convenient tool for thermotherapy since they may provide controllable local heating and contactless temperature sensing at the same time.[15–18]

In this work, we developed a simple method for the preparation of Ag_2S nanoparticles capped with thioglycolic acid (TGA) in aqueous media though a facile one-pot approach. The prepared nanoparticles were characterized using different spectroscopic techniques including XRD, FTIR, TEM imaging, EDS, UV-vis absorption and photoluminescence. These nanoparticles were used *in vitro* experiment to explore their infiltration on U-87 MG (glioblastoma) living cells and to demonstrate their performance for fluorescence imaging and temperature sensing. We have also performed a detailed toxicity analysis evaluated throw MTT assay protocol.

2. Experimental section

2.1. Chemicals

Silver nitrate ($AgNO_3$), thioglycolic acid ($HSCH_2COOH$), sodium sulfide (Na_2S) and sodium hydroxide (NaOH) were purchased from Sigma-Aldrich. All these reagents were of analytical grade and were used without any further purification. Distilled water was used as solvent in the synthesis experiments.

2.2. Preparation of TGA-capped Ag_2S nanoparticles

Silver sulfide nanoparticles encapsulated with thioglycolic acid (TGA) were prepared using a modified colloidal wet chemical route as described in[19]. Thioglycolic acid (TGA) was used as capping agent to control the size of Ag_2S nanoparticles and to prevent their agglomeration and sedimentation due to its strong interaction with silver. Indeed, the low solubility of Ag_2S leads to the rapid formation of large particles or unwanted precipitates. The molar ratio of Ag/S/TGA chosen in this synthesis was 1/0.25/2. The experimental synthesis protocol is briefly described as follows. Firstly, we dissolve in a three necked flask 1.5 mmol of $AgNO_3$ and 3 mmol of the capping agent (TGA) in 75 mL of distilled water. A solution of NaOH (1 M) was added dropwise to the initial solution to adjust the pH to 11. Thiol molecules react strongly with silver ion to give Ag-TGA complexes which act as new reaction precursors. After that, the mixture was stirred magnetically and degassed in the presence of N_2. Secondly, a solution of 0.375 mmol of Na_2S in 25 mL was injected into the solution containing Ag-TGA complexes at room temperature. After that, the mixture was heated up to 100 °C for 2 h leading to the progressive coloration of the solution from light yellow to dark-brown or almost black indicating the formation of Ag_2S nanoparticles. This happens due to the slow release of Ag^+ ions which react with silver ions to give small Ag_2S nanoparticles which grow continuously. Finally, the reaction mixture was cooled down to room temperature then purified by precipitation and washing with ethanol. Then the samples were stored for eventual applications in atmospheric environment at 4 °C.

2.3. Morphology and structural and chemical analysis

The morphology, average size and chemical composition of Ag_2S nanoparticles were analysed by using a transmission electron microscope (TEM, JEOL JEM 1400 Flash) or a high resolution transmission electron microscope equipped with energy-dispersive X-ray (EDS) spectrometer (JEOL JEM 2100 (HRTEM)). Thus, a colloidal solution of Ag_2S nanoparticles was dropped on a copper grid and dried in air at room temperature before introduced into TEM or HRTEM apparatus. The EDS quantification was carried out using the *K* factor of Sulfur K line and Silver L line transitions. Fourier-transform infrared (FTIR) were obtained in transmission mode in the 400–4000 cm^{-1} range by preparing KBr tablets containing the powder of Ag_2S nanoparticles. X-Ray powder diffraction (XRPD) measurements were performed by using a Philips X'pert PRO MPD Panalytical diffractometer, working in the Bragg–Brentano geometry (θ–2θ) in the 20–60° range and using filtered CuKα radiation ($\lambda = 1.542$ Å). The hydrodynamic diameter was measured by dynamic light scattering (DLS) spectroscopy using a Zetasizer Ultra (Malvern Panalytical, Ltd) apparatus.

2.4. PL measurements

For cell thermometry, we have first measured the PL emission spectra of Ag_2S nanoparticles at different temperatures. To monitor the temperature, a small cuvette containing 1 mL of an aqueous solution of Ag_2S nanoparticles (0.5 mg mL^{-1}) were placed inside a spectrometer sample compartment (qpod 2e, Quantum Northwest), where the temperature of the cuvette holder is regulated by an internal controller. The emission spectrum is collected by small spectrometer (Ocean Optics) under 488 nm laser excitation. Temperature has been changed between 15 and 50 °C, with 5 °C steps. Photostability experiment was performed by recording the PL emission of Ag_2S nanoparticles dispersed in an aqueous solution in small cuvette at room temperature under continuous illumination at an

excitation wavelength of 488 nm and a fixed laser power of 5 mW following different irradiation periods.

The pH was controlled by adding 0.5 mg of Ag_2S nanoparticles to a buffer solution prepared by dissolving the adequate quantities of KH_2PO_4 and NaOH in 1 mL of deionized water. The ionic strength was modified by dissolving the convenient quantity of KCl salt in 1 mL of an aqueous solution containing 0.5 mg of Ag_2S nanoparticles.

2.5. Cell lines and culture conditions

The cell line (U-87 MG) is derived from epithelial human tissue, specifically from brain human cancer (glioblastoma). Cells were grown as a standard monolayer culture, in Dulbecco's Modified Eagle's (DMEM) supplemented with 10% Fetal Bovine Serum (FBS) and 1% Penicillin-Streptomycin (10 000 U mL^{-1}, P/S). All reagents were purchased from Cytiva. Cells' population was routinely regulated in 25 cm^3 under controlled conditions (at 37 °C in a humidified atmosphere of 5% CO_2).

2.6. Viability assays

Cytotoxicity of the Ag_2S against U-87 MG cells is evaluated *via* MTT viability assay, which measures the levels of cell metabolic activity. Cells were grown in 24 well-plate for 48 h (at 37 °C in a humidified atmosphere of 5% CO_2) to allow them to reach 80–90% of confluence. Then, the medium is replaced by new medium containing 3, 6, 15 and 30 μL of Ag_2S nanoparticles dispersed in phosphate buffered saline solution (PBS), corresponding to concentrations of 10, 20, 50 and 100 μg mL^{-1} respectively. The nanoparticles were incubated with the cells for 2 and 24 h. Moreover, a negative control of medium and medium containing 30 μL of PBS has been made. After the incubation time, this medium was exchanged with a solution of 90% fresh medium and 10% of MTT (1 mg mL^{-1}) resulting a final solution of 500 μL in each well. After 2 h of incubation, the solution is extracted and 500 μL of DMSO (dimethyl sulfoxide) is added to each well, dissolving the formazan crystals formed because of the metabolic activity of the cells and finally the absorbance of each well can be read.

2.7. PL imaging of cells

For PL imaging, around 40.000 of (U-87 MG) cells were cultured in 35 mm confocal dish, incubated at 37 °C with 5% CO_2. After 48 h, these cells were incubated with Ag_2S nanoparticles (5 μL, 10 μg mL^{-1}) (10 μL, 20 μg mL^{-1}) and (25 μL, 50 μg mL^{-1}) at 37 °C with 5% CO_2 for 24 h. After that, cells were washed 3 times by PBS to remove extra nanoparticles, then 2 mL PBS were added into the dishes to keep bio-environment and avoid dryness. One heating plate was using for temperature control, and a thermocouple was used to monitor the real temperature. PL images of cells under different temperature were collected by a fluorescent microscope.

3. Results and discussions

3.1. Structural characterization of Ag_2S/TGA NPs

3.1.1 FITR spectrum. To inspect the molecular interaction between Ag_2S nanoparticles and the capping agent TGA, we have recorded the FTIR spectrum of the prepared Ag_2S nanoparticles (Fig. 1). We can note the disappearance of the peak corresponding to the thiol group (S–H) of TGA, which usually appears between 2565 and 2677 cm^{-1}.[20] This reveals the breaking of the S–H bond. Fig. 1, shows also two peaks situated at 1569 and 1387 cm^{-1} that can be assigned respectively to the asymmetric and symmetric vibrations of the carboxylic groups (COO^-). This means that TGA molecules are adsorbed on the Ag_2S surfaces in the ionic form with a free carboxylic terminal group COO^-. The absorption band at 716 cm^{-1} is attributed to (C–S). The bands at 775 and 1215 cm^{-1} correspond to (C–S) and (CH_2), whereas the band at 927 cm^{-1} is related to OH in COOH.[21] The appearance of the bands specific of TGA together with the simultaneous disappearance of the band characteristic of thiol group (S–H) indicates the fixation of the TGA on the surface of Ag_2S nanoparticles due the electrons pair on the sulfur, which interact strongly with silver.[22]

3.1.2 XRD analysis. The crystal structure of the formed Ag_2S/TGA nanoparticles powder was examined by X-ray diffraction (XRD). As can be seen in Fig. 2, the XRD pattern is constituted of large bands without clear diffraction peaks, which indicates the formation of crystals with very small sizes. Moreover, according to the authors of ref. 23, this is a characteristic of the monoclinic lattice of Ag_2S which has abundant reflections (see in Fig. 2, the 2θ angles relative to the different diffraction planes according to the JCPDS 00-014-0072 pattern). For small sizes, the diffraction signals broaden and overlap to form a wide halo in the 2θ angle range from 10° to 50°. At the same time, the amorphous thiol shell at the surface of nanoparticles may hide the crystal peaks.[5]

3.1.3 Morphology and size distribution. TEM image of Fig. 3a preformed on TGA-capped Ag_2S NPs shows the presence of spherical particles. Some of these nanoparticles were agglomerated, which may be due to the evaporation of solvent.[24] The size distribution histogram of the as-prepared Ag_2S NPs showed an average diameter of nearly 3.4 nm (Fig. 3b). We note

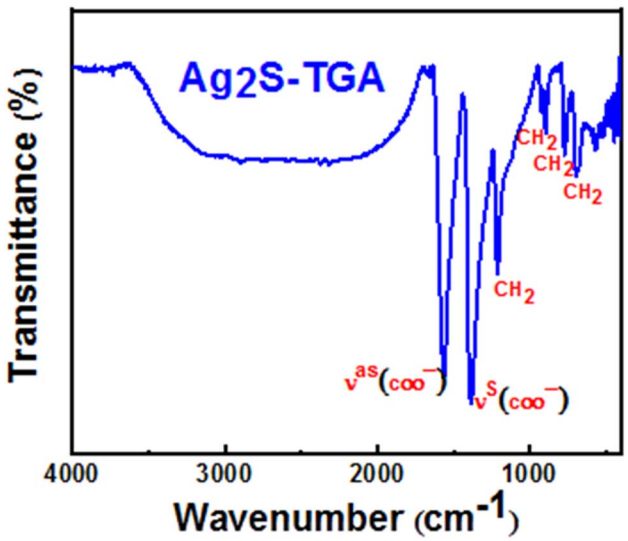

Fig. 1 FTIR spectrum of TGA-Ag_2S nanoparticles.

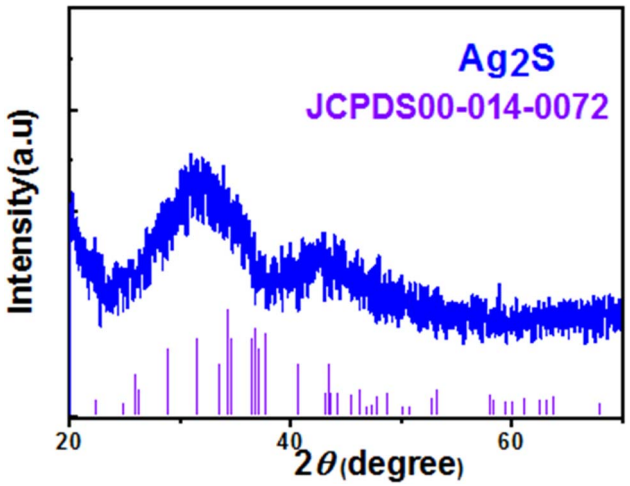

Fig. 2 XRD powder pattern of TGA-Ag_2S nanoparticles.

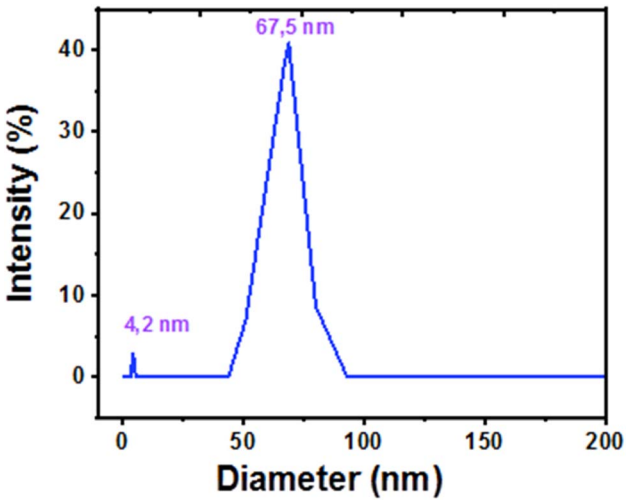

Fig. 4 DLS histogram of TGA-Ag_2S nanoparticles dispersed in water.

however, that TEM images revealed the presence of two populations of particles having very different averages sizes, which may be assigned to individual small nanoparticles and large particles formed by the agglomeration of a great number of nanoparticles (see Fig. S1 in the ESI†). The high-resolution TEM image (HR-TEM) in Fig. 3c shows the diffraction from the (−112) crystallographic planes of the Ag_2S monoclinic crystal lattice with *d*-spacing of 0.285 nm (JCPDS standard card 00-014-0072 of Ag_2S).

3.1.4 DLS spectra. Prior to DLS measurements, Ag_2S nanoparticles was first uniformly dispersed in water using ultrasonication. The DLS histogram of a sonicated solution represented in Fig. 4 exhibits bimodal distribution of agglomerates which reveals the presence of two populations of Ag_2S nanoparticles with different average sizes in accordance with the results obtained from TEM images analysis. The small average size of 4.2 nm is greater than that deduced from TEM image analysis. The large average of 67.5 nm may be associated to agglomerates of individual small nanoparticles. The signal at this average diameter has the highest intensity which can be explained by the fact that DLS is more sensitive to large particles

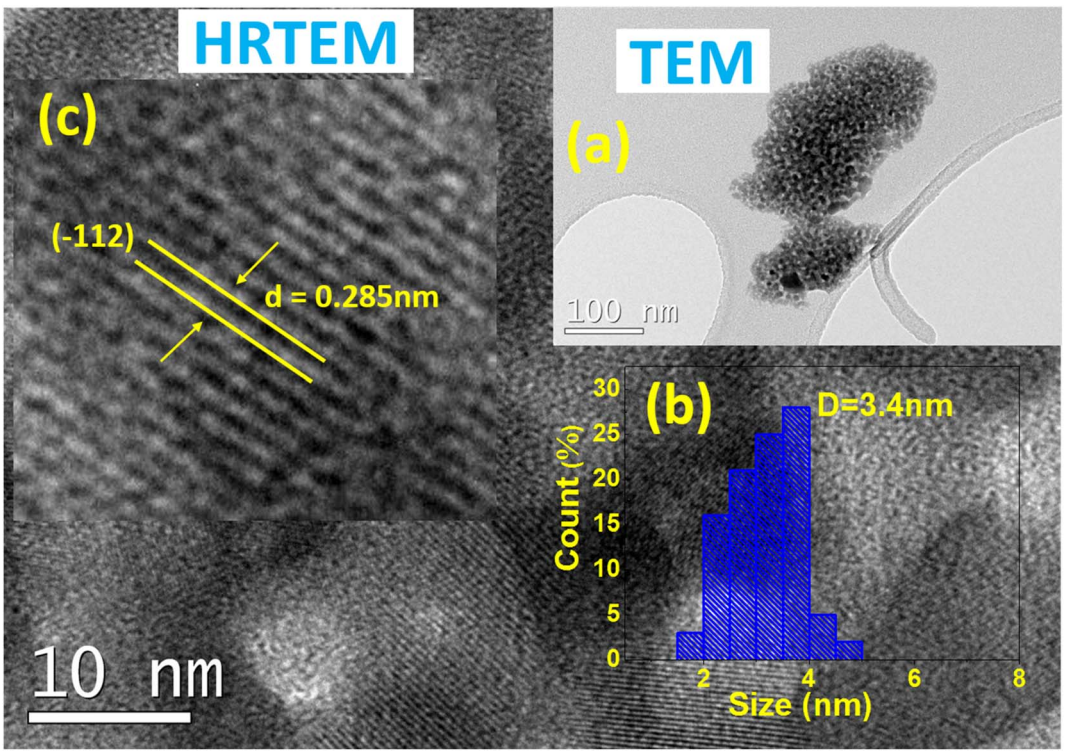

Fig. 3 TEM (a) and HRTEM images (c) and size distribution histogram (b) of TGA-Ag_2S nanoparticles extracted from TEM image.

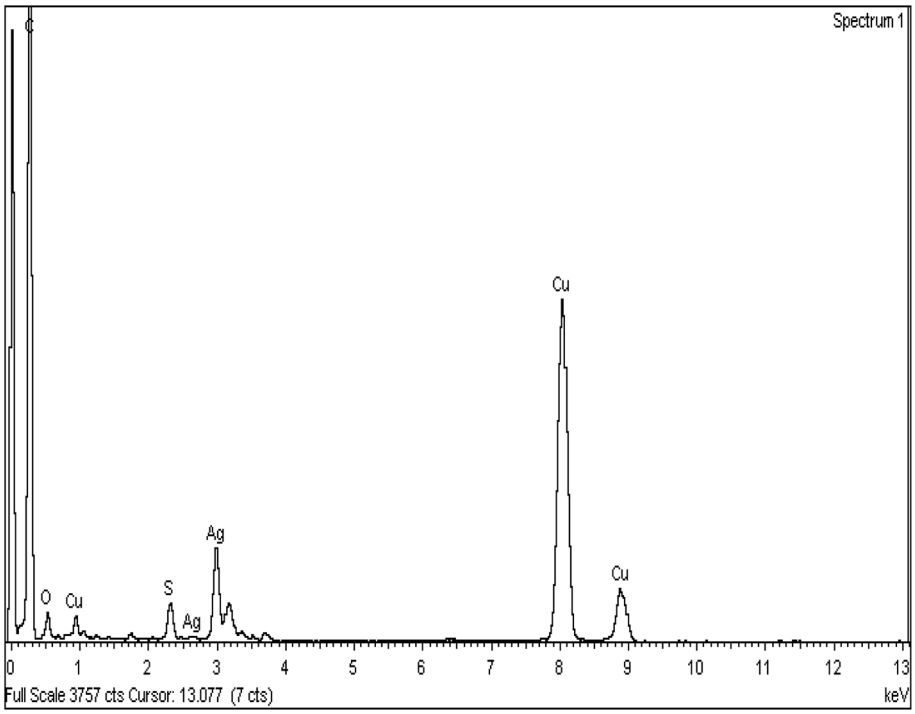

Fig. 5 EDS spectrum indicating the atomic composition of TGA-Ag_2S nanoparticles.

and agglomerates because these particles scatter much more light and even a small number of large particles can obscure the contribution from smaller particles.[25] The presence of such large agglomerates may be due to the dilution which induces the detachment of the ligand and results in the aggregation of the dispersed nanoparticles.[26] The aggregation of the nanoparticles may be also due to the interaction and interdigitation of thiol molecules throw hydrogen bonds between their terminal groups. Additionally, it was suggested that sonication may act against the repining effect of thiol ligand, which causes noticeable aggregation at longer time of sonication.[24]

3.1.5 EDS analysis. We have performed an EDS analysis to get information about the elemental composition of the synthesized Ag_2S nanoparticles. From the EDS spectrum in Fig. 5, we observe the existence of the principal elements, which are sulfur and silver. In addition, we can note the presence of carbon and oxygen coming from thiol capping agent. We may observe also, the presence of copper which may come from the grid. The ratio Ag/S estimated from EDS measurements is equal to 2.2, which is slightly higher than the theoretical ratio 2.0 corresponding to perfect Ag_2S crystal (Table 1). This result is consistent with the calculations of the authors of ref. 27 who demonstrated that an excess of silver will be present in silver sulphide nanoparticles, even if prepared in the presence of a sulphide ion excess. Similar results were also reported for Ag_2Se nanoparticles.[28] The presence of such silver excess would indicate the possible presence of defects in the nanoparticles and on their surfaces.

Table 1 Chemical composition of TGA-Ag_2S nanoparticles extracted from EDS analysis

Element	Peak area (a.u.)	*k* factor	Weight (%)	Weight (%)	Atomic (%)
S K	1251	0.959	11.87	0.72	31.17
Ag L	5092	1.757	88.13	0.72	68.83

3.2. Optical properties of Ag_2S/TGA NPs

3.2.1 Optical absorption. In Fig. 6, we have presented the absorption spectrum of TGA-capped Ag_2S nanoparticles. This

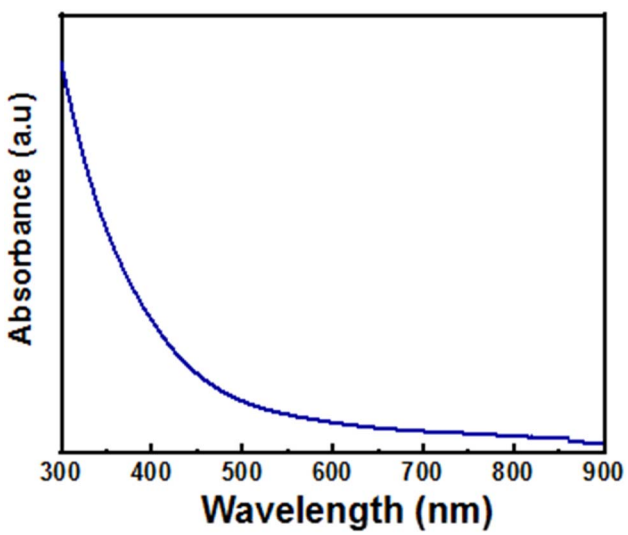

Fig. 6 Optical absorption spectrum of TGA-Ag_2S nanoparticles dispersed in water.

figure shows an increasing absorption when increasing the photon energy with a featureless tail with no distinctive peak corresponding to the absorption relative to the ground exciton state like those observed for II–VI semiconductor's nanoparticles. This may be attributed to the defect-related transitions, which overlap with excitonic transition, obscuring thus the excitonic absorption band.[29] Others origin of such future, may be the special difference between the electronic properties of silver sulfide and II–VI semiconductor nanocrystals or the inhomogeneous composition and size distribution of the ensemble of the nanocrystals.

Since the optical spectrum does not exhibit a clear excitonic peak, we have used the second derivative method to estimate the bandgap energy of the prepared Ag_2S nanoparticles (Fig. S2 in the ESI†). The wavelength corresponding to the peak of the second derivative of the absorption spectrum is $\lambda_a = 860$ nm, which is largely blue shifted relative to the absorption edge for bulk Ag_2S crystals (~1240 nm). This result indicates that the prepared Ag_2S nanoparticles may be excited in the first biological window by using NIR radiations, which is ideal for PL imaging. The bandgap energy was obtained from value of λ_a by using equation:

$$E_g\ (\text{eV}) = \frac{1240}{\lambda_a} \quad (1)$$

The obtained value was equal to 1.44 eV, which is larger than the bandgap energy of bulk Ag_2S (~1 eV). This indicates that the synthesized nanoparticles are sufficiently small to exhibit the so-called quantum confinement effect of the charge carriers.

We have also estimated the nanoparticles radius, R from the experimental band gap energy by using the so-called effective mass approximation according to the following Brus equation:[30]

$$E_g(\text{QDs}) = E_g(\text{bulk}) + \frac{h^2}{8R^2}\left(\frac{1}{m_e} + \frac{1}{m_h}\right) - \frac{1.8e^2}{4\pi\varepsilon_0\varepsilon_r} \quad (2)$$

In the above equation, h is the Planck constant, ε_0 is the vacuum permittivity and E_g(QDs) and E_g(bulk) are the respective bandgap energies of Ag_2S nanoparticles and bulk Ag_2S. The effective masses of electrons and holes are respectively equal to $m_e = 0.286 \times m_0$ and $m_h = 1.066 \times m_0$ and $m_0 = 9.0195 \times 10^{-31}$ kg is the free electron mass. The relative permittivity of silver sulfide is equal to $\varepsilon_r = 5.95$. From Brus equation, we may estimate the size of the nanoparticles by using the following equation:[31,32]

$$R = \frac{\left(\frac{1.8e^2}{4\pi\varepsilon_0\varepsilon_r}\right) + \sqrt{\left(\frac{1.8e^2}{4\pi\varepsilon_0\varepsilon_r}\right)^2 + \left(E_g(\text{QDs}) - E_g(\text{bulk})\right) \times \frac{h^2}{2m_0}\left(\frac{1}{m_e} + \frac{1}{m_h}\right)}}{2\left(E_g(\text{QDs}) - E_g(\text{bulk})\right)} \quad (3)$$

The obtained radius of the nanoparticles was equal to 2.3 nm which is of the same order of Bohr radius for bulk Ag_2S (~2.2 nm) and clearly shows that the synthetized nanoparticles are in the intermediate confinement regime. The small difference between the average sizes obtained from Brus equation and TEM analysis can arise due to assumptions made in the Brus equation such as the nanoparticles being spherical and homogeneous and the presence of size distribution in the sample. Additionally, the artifacts produced during preparation steps of the sample for TEM imaging may alter the nanoparticle size or shape. Moreover, TEM gives us access only to a very small domain which could hide the full size distribution over all the sample.

3.2.2 Photoluminescence analysis

3.2.2.1 Origin of the PL emission. Fig. 7 shows a typical photoluminescence spectrum of a colloidal solution of Ag_2S NPs dispersed in water and recorded under an excitation wavelength equal to 488 nm. By comparing this emission of Ag_2S nanoparticles, which appears in this spectral region between 720 and 1000 nm with a maximum at 915 nm to those obtained in other recent studies, we may suggest that these particles are very small and behave as quantum dots in accordance with the results deduced from the optical study. Fig. 7 shows also that the emission band is asymmetric with a less steep low-energy side and a bandwidth of nearly equal to 130 nm. Thus, we have convoluted this PL spectrum by two Gaussian components peaking at nearly 915 and 980 nm. These bands may be assigned respectively to direct exciton recombination and transitions involving defect states in the band gap. Indeed, similar to many semiconductor nanocrystals, defect states such as vacancies, impurities, or lattice strain, can be created inside and at the surface of the nanocrystals during the synthesis process. The effect of such defect states is more pronounced especially in small nanocrystals which are characterized by a high surface to volume ratio. The asymmetry of the PL spectra may also come from two populations of Ag_2S nanoparticles with different averages sizes which seems to be in agreement with the analysis of TEM and DLS measurements. Indeed, it is basically extremely difficult to produce a perfectly monodisperse nanocrystals population. However, the overall emission of these nanoparticles falls within the NIR-I window, which is convenient for biomedical imaging and therapeutic applications due to the high depth penetration into biological tissues of such IR radiations due to the low absorption and scattering of light in this spectral region.[33]

3.2.2.2 Effect of temperature on the PL emission. The PL spectra of Ag_2S nanoparticles were recorded in the physiological temperature range (15–50 °C) and they are represented in Fig. 8, which reveals an important thermal quenching of the emission whereas the emission wavelength and bandwidth remain nearly temperature independent. This indicates the thermal stability of the emission of these nanoparticles which may be suitable for bio-imaging application. Several parameters may be involved in

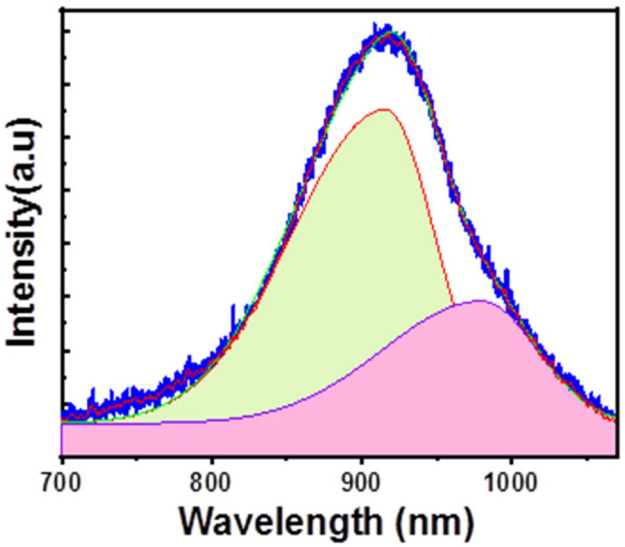

Fig. 7 Typical PL spectrum of TGA-Ag_2S nanoparticles dispersed in water and recorded at room temperature under 488 nm excitation wavelength.

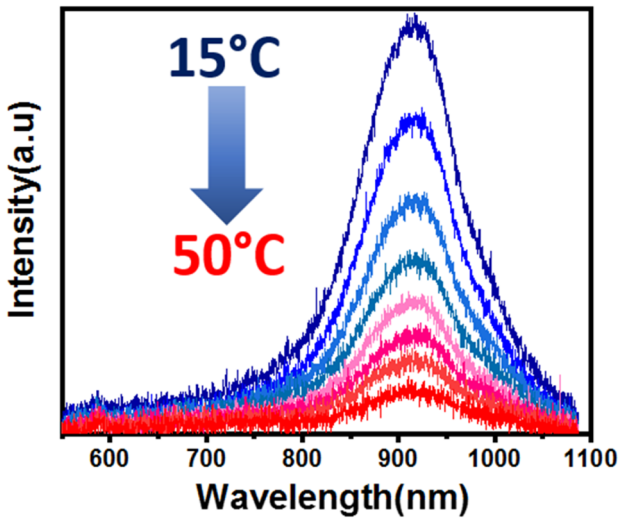

Fig. 8 Evolution with temperature of the PL emission of TGA-Ag_2S nanoparticles dispersed in water and recorded under 488 nm excitation wavelength.

the thermal quenching of the emission including electron–phonon coupling, defects or impurities. Indeed, the mobility of atoms or ligand molecules at the surface of the nanoparticles when increasing temperature can lead to the formation of new thermally activated surface states or changes in the surface chemistry.[34,35] Another factor that influences the nanoparticles emission is the strain induced by the thermal mismatch between Ag_2S nanoparticles and their capping agent and the solvent. However, the almost constant emission wavelength and bandwidth may be attributed to the opposite effects of lattice expansion and defect states and electron–phonon coupling which results in complex behavior of the emission process. Indeed, thermal expansion of the lattice may induce a blue shift whereas defects and electron–phonon coupling often gives a redshift of the emission.[36] However, the fact that the bandwidth of the emission band did not show a considerable variation with temperature indicates that thermal effects such as thermal expansion and electron–phonon coupling are negligible. Therefore, the main contribution to the emission broadening is attributed to an intrinsic inhomogeneity stemming from fluctuations in the size, shape and composition of Ag_2S nanoparticles, which is temperature independent. Indeed, it was reported that the broadening of the emission with increasing temperature is mostly due to the electron–phonon coupling (homogenous broadening) which is observed even within a perfectly monodisperse size distribution whereas the inhomogeneous broadening is nearly temperature independent.[37] Moreover, the fact that the PL spectrum preserves the same shape when varying the temperature may indicate that the ratio between the two populations of Ag_2S nanoparticles is thermally stable.

To further elucidate the origin of the photoluminescence thermal quenching, we have also reproduced the emission spectra when cooling down the solution containing Ag_2S nanoparticles to room temperature. Fig. 9 shows the evolution with temperature of PL intensity at the maximum emission wavelength. We have obtained the same trend of the integrated area of the emission band in the whole wavelength range (see Fig. S3 in the ESI†). This figures demonstrate that the two plots obtained under heating and cooling recover indicating a totally reversible quenching process of the emission in the whole investigated temperature range. Such thermal quenching may be due to the reversibly formed trap states at the ligand/nanocrystals interfaces or to pre-existing traps that become thermally accessible. Such behaviour of the PL quenching may be due to the strong interaction between thiol molecules and silver atoms at the surfaces of the nanocrystals which prevents

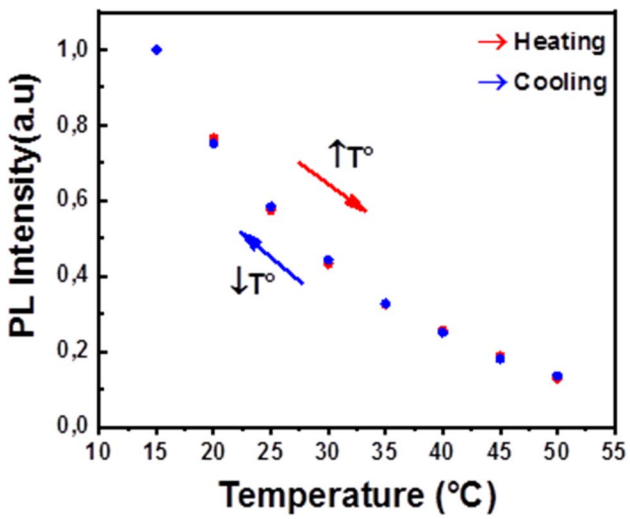

Fig. 9 Evolution of the PL intensity of TGA-Ag_2S nanoparticles dispersed in water and recorded for heating and cooling cycle under 488 nm excitation wavelength.

ligand desorption that leads to unpassivated surfaces and irreversible photoluminescence quenching.[38] Indeed, Ag^+ ion is a very soft Lewis acid whereas TGA is a very soft base which makes from it a very effective stabilizing agent for Ag_2S nanoparticles.[39]

3.2.2.3 Evolution of the PL decay with temperature. Lifetime measurements may also provide insights into the physical processes that cause thermal fluorescence quenching observed in this study. Therefore, we have recorded the PL decay at the maximum emission wavelength as a function of temperature. Fig. 10 shows a typical PL decay plot which deviates from the exponential behaviour indicating the complexity of charge carriers' recombination process. Therefore, we fitted the PL decay curves to a sum of two exponential functions according to the following formula:

$$I(t) = A_1\, e^{-\frac{t}{\tau_1}} + A_2\, e^{-\frac{t}{\tau_2}} \quad (4)$$

In this equation, τ_1 and τ_2 represent the short and long components of the photoluminescence decay and A_1 and A_2 are the relative amplitudes of the two components. Indeed, we have obtained a reasonable fit of the PL decay (with *R*-squared, $R^2 \sim 0.99$) only for temperatures below 25 °C whereas for higher temperature, the signal became weak and very noisy which makes the fitting very difficult. We note however, that the short component of the PL decay decreased slowly when increasing the temperature and didn't exceed 4 ns whereas the slow component is shorter than 20 ns (Table 2). Many controversy explanations of the PL decay of semiconductor nanoparticles were given in recent literature, which indicates the complexity of carrier recombination dynamics behind this PL decay. Some authors associate the short component τ_1 to recombination involving charge traps whereas the long decay component τ_2 is attributed to direct exciton recombination.[40,41] Accordingly, the measured decay lifetimes are a mixture of both exciton and trap-state dynamics. Others researchers attribute the long lifetime component to larger nanoparticles and the short one to the small nanoparticles which may have more surface defects and non-radiative recombination centers. This leads to decrease the photoluminescence lifetime further. Moreover, the fact that the photoluminescence decay of these Ag_2S nanoparticles is faster than that observed in others previous studies and its variation with temperature is small, reinforces the assumption that the measured lifetimes are related to intrinsic excitonic emission originating from two Ag_2S nanoparticles populations rather than defect-related emission.[41] Furthermore, the fact that A_1 is greater than A_2 especially for temperature below 25 °C, indicates that the important part of the emission intensity comes from the smaller nanoparticles where the radiative transitions are more probable, and thus radiative decay time is shorter. According to ref. 42, this quenching occurs due the formation of "dark nanoparticles" whose fraction increases with rising temperature. Such nanoparticles, which contribute to light absorption but not to emission, result from thermal promotion of valence band electrons to unoccupied surface states leaving the core of the particle positively charged and hence dark. These nanoparticles do not affect the total PL decay because their nonradiative relaxation occurs in a timescale shorter than the time resolution of the experimental setup.

Table 2 PL decay parameters estimated from the fitting of the decay of the maximum PL intensity of TGA-Ag_2S nanoparticles recorded at different temperature under an excitation wavelength of 488 nm

T (°C)	A_1	τ_1 (ns)	A_2	τ_2 (ns)
15	1.04	3.49	0.05	17.22
20	1.07	3.16	0.03	19.03
25	1.06	2.71	0.05	13.28

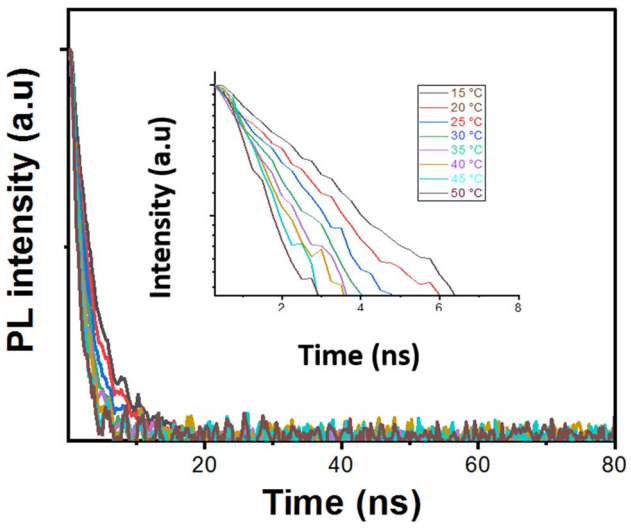

Fig. 10 Evolution of the PL decay recorded at the maximum emission wavelength for different temperatures under an excitation wavelength equal to 488 nm. The inset plot shows the evolution with temperature of the of PL decay at shorter times after the excitation of TGA-Ag_2S nanoparticles.

Taking in consideration the difficulty to explain the behaviour of the PL decay, we think that further theoretical investigations must be done to acquire full understanding of the temperature dependence of the PL decay of Ag_2S nanoparticles and the role of the solvent and the ligand attached on their surface on their optical properties. It is worth to note however, that although the PL emission exhibits a short lifetime, these Ag_2S nanoparticles may be convenient for some applications involving fast-moving images to prevent afterglow that blurs the display.

3.2.2.4 Photostability and photobleaching resistance. The PL spectra shown in Fig. 11 reveal that the PL position and bandwidth are not significantly affected by photoirradiation duration whereas the PL intensity shows a small increase which indicates that Ag_2S coated by TGA molecules are photostable and highly resistant to photo-oxidation and photobleaching. The increase of the PL intensity may due to a partial passivation of surface defects which acts as recombination sites of the photogenerated charges carriers.[43]

3.2.2.5 Effect of storage time, pH and ionic strength on the PL emission. We have reproduced the PL spectra in the same

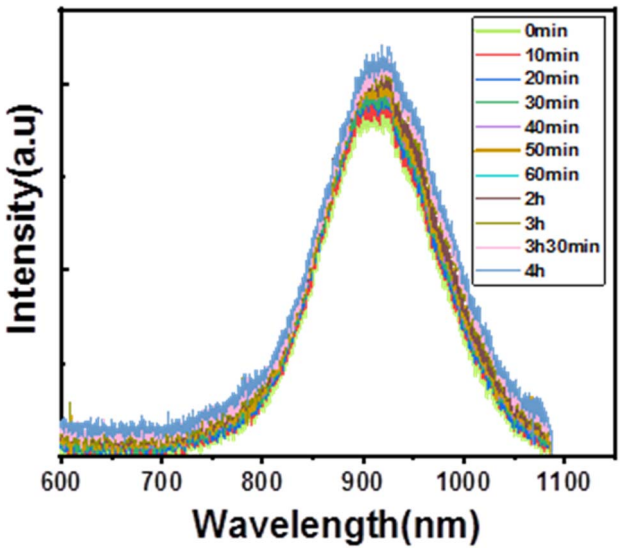

Fig. 11 Evolution of the PL emission of TGA-Ag_2S nanoparticles with the irradiation duration recorded at room temperature under an excitation wavelength of 488 nm and source power of 5 mW.

conditions of freshly prepared Ag_2S nanoparticles and those stored for 6 months and one year. As it can be noticed from Fig. 12a, the PL emission shows a slight decrease after 6 months of storage whereas the spectrum recorded after one year exhibits a more pronounced decrease of the PL intensity. Additionally, no significant spectral shift or broadening of the emission band were observed, which reveals the stability of these nanoparticles for a storage time at least equal to 6 months in atmospheric environment at 4 °C.

Because the pH and ionic strength within a living cell are highly varying, it is of great importance to assess the behaviour of the PL emission of Ag_2S nanoparticles if we want to use them for optical thermometry and fluorescence imaging of living medium. Therefore, we have investigated the effect of pH and ionic strength on the PL emission of Ag_2S nanoparticles dispersed in aqueous solutions having different pH and ionic strength values.

The obtained results shown in Fig. 12b indicate that the position of the PL emission remains constant whereas the PL intensity increases with increasing the pH of the solution although it remains nearly constant in the physiological pH range between 6.8 and 7.4. This increase of the PL intensity of Ag_2S nanoparticles may be due to their well shielding by thiol molecules which are strongly fixed to their surface. Indeed, it was reported that at intermediate pH values, the interaction between sulphur based semiconductor nanoparticles and a thiol capping agent is strong enough whereas the detachment of thiol molecules appears at low pH values due to the interaction of hydrogen ions (H^+) with ligand molecules which results in their detachment and the aggregation of Ag_2S nanoparticles.[44,45]

We can see from Fig. 12c, that when increasing the concentration of KCl, the PL emission intensity increases until it reaches its maximum value for a concentration of 150 mM

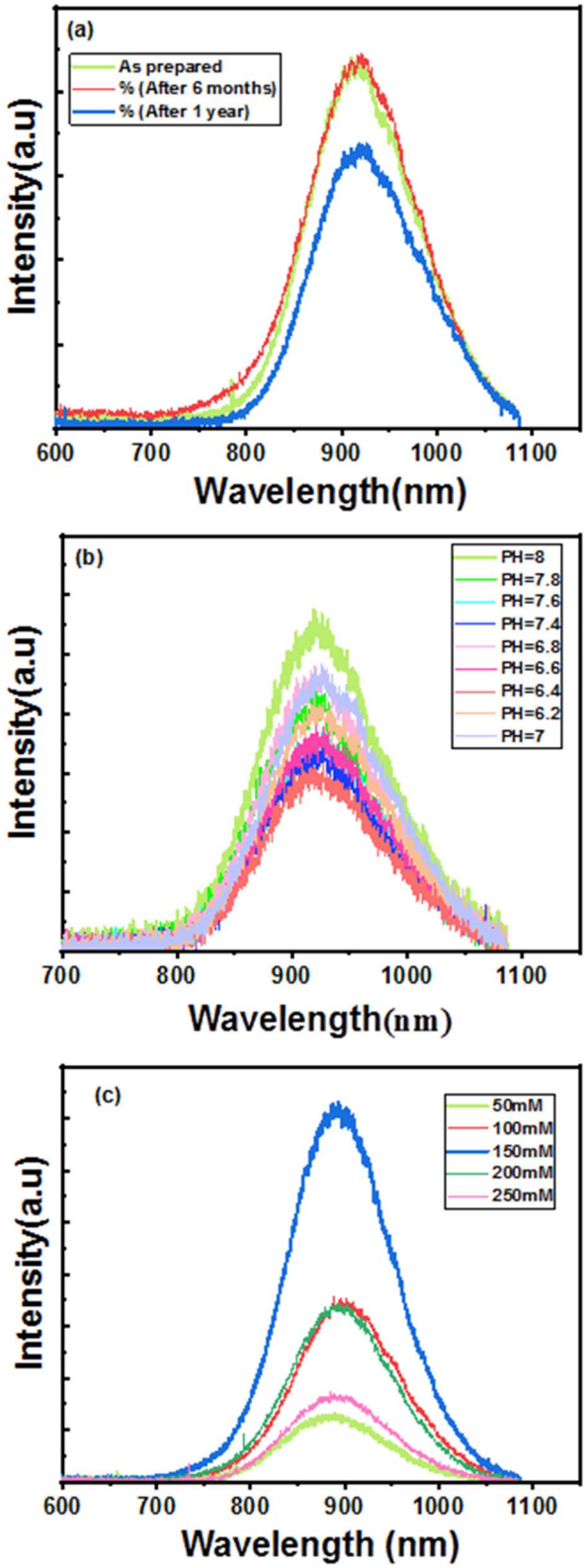

Fig. 12 (a) Effect of storage time on the PL emission of TAG-Ag_2S nanoparticles. (b) Effect of the solution pH on the PL emission of TGA-Ag_2S nanoparticles. (c) Effect of KCl concentration on the PL emission of TGA-Ag_2S nanoparticles.

before decreasing. This feature is highly required because the total ion concentration in the cytoplasm is equivalent to 150 mM.[46] We may notice however a small blue shift for concentrations higher than 150 mM.

3.3. Application of Ag_2S nanoparticles for cell imaging and temperature sensing

3.3.1 Evaluation of cytotoxicity of TGA-coated Ag_2S NPs by MTT assay. Before using Ag_2S nanoparticles in any subsequent application in living cells, we have investigated their effect on the viability, proliferation and cytotoxicity of U-87 human malignant cells by using the conventional MTT protocol. Therefore, the cells were incubated for 2 h and 24 h with different concentrations (10–100 μg mL^{-1}) of Ag_2S nanoparticles in a culture medium. An assay containing only cells in the same volume of culture medium were used as assay control for each time test. Cells viability and cytotoxicity of Ag_2S nanoparticles were evaluated by measuring the absorbance at 500–600 nm using a multi-well spectrophotometer. The cell survival rate was therefore determined by the following equation:[47]

$$\text{Cell survival rate } (\%) = \frac{\text{absorbance of test cells}}{\text{absorbance of control cells}} \times 100 \quad (5)$$

As we can see in Fig. 13, the results showed that more than 80% of the cells retain their activity after being exposed to different concentrations of Ag_2S nanoparticles for 24 h. From these results we can conclude that Ag_2S nanoparticles possess low cytotoxicity, which reveals their biocompatibility and makes of them suitable for living cell imaging and others medical applications.

3.3.2 Cell imaging. Cell (U-87) incubated with 20 μg mL^{-1} of Ag_2S-TGA nanoparticles for 24 h were imaged by using a fluorescence microscope under an excitation wavelength equal to 488 nm. If we compare the two images of Fig. 14, we can see that the optical signal originating from Ag_2S nanoparticles demonstrated with red colour is dramatically higher inside the cells which confirms their efficient internalization and localization within the entire cellular cytoplasm. We can therefore suggest that the synthesized Ag_2S nanoparticles, which possess very low cytotoxicity, high absorption and bright emission in the NIR region may be used as fluorescent probes for cell imaging and disease diagnosis of the biological medium. However, the properties of these nanoparticles such as their size, water dispersibility, NIR fluorescence and their specific targeting for drug delivering, may be further improved by choosing a convenient method to functionalize their surface.

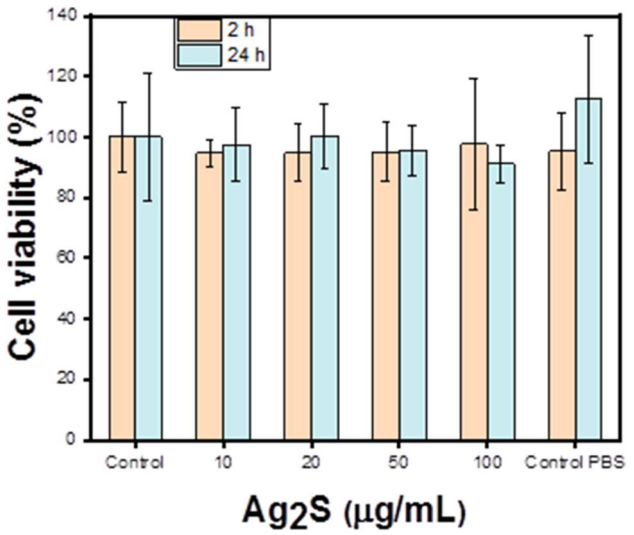

Fig. 13 Cytotoxicity results obtained by MTT assay to U-87 human living cells exposed to different concentrations of TGA-Ag_2S nanoparticles for two hours and 24 hours.

3.3.3 Temperature sensing. The reversible thermal quenching of the PL signal demonstrates that the prepared Ag_2S nanoparticles may be used as stable tool for temperature sensing by calibration of the emission intensity or area. The reversibility of the measurement is demonstrated in Fig. 9 which shows a recovery of the two curves obtained under heating and cooling. However, to compare our results with those recently reported, we have calculated the relative thermal sensitivity S_r, which is one of the most important parameter for characterizing luminescent thermometers. This sensitivity is estimated by using the following formula:[48,49]

$$S_r = \frac{1}{R} \times \left|\frac{dR}{dT}\right| \quad (6)$$

In this equation, R represents either the intensity or the integrated area of the emission and dR expresses the change in this parameter with change of temperature, dT. From the analysis of the experimental data, we have found that the relative thermal sensitivity is nearly constant between 15 and 40 °C whereas it varies (in % per °C) from 5.5 at 40 °C to 12.2 at 50 °C (see Fig. S4 in ESI†). These values are of the same order and even higher than those recently reported for fluorescent nanothermometers,[24,50–52] which makes of the as-prepared nanoparticles convenient for temperature sensing operating in the NIR biological windows. However, the shape, the position and the intensity of the emission of Ag_2S nanoparticles may be influenced by water absorption, which depend on temperature. Additionally, photoexcitation intensity and unwanted light-induced heating of the sensed medium may affect the emission of the nanoparticles. Therefore, it is necessary to consider such effects on the accuracy of temperature measurement when using Ag_2S nanoparticles for temperature sensing in the biological medium.

The evolution with temperature of the PL intensity coming from Ag_2S nanoparticles dispersed in water have encouraged us to try to investigate the temperature variation inside the cells by using an infrared camera. Therefore, we have imaged the fluorescence of living cells in the temperature range from 24.1 °C to 39.3 °C Fig. 15 and (see Fig. S5 in ESI†). From these images we have extracted the resulting PL intensities from different cells and we have recorded their evolutions with temperature Fig. 16 and (see Fig. S6 in ESI†). These figures shows that PL emission decrease when increasing temperature

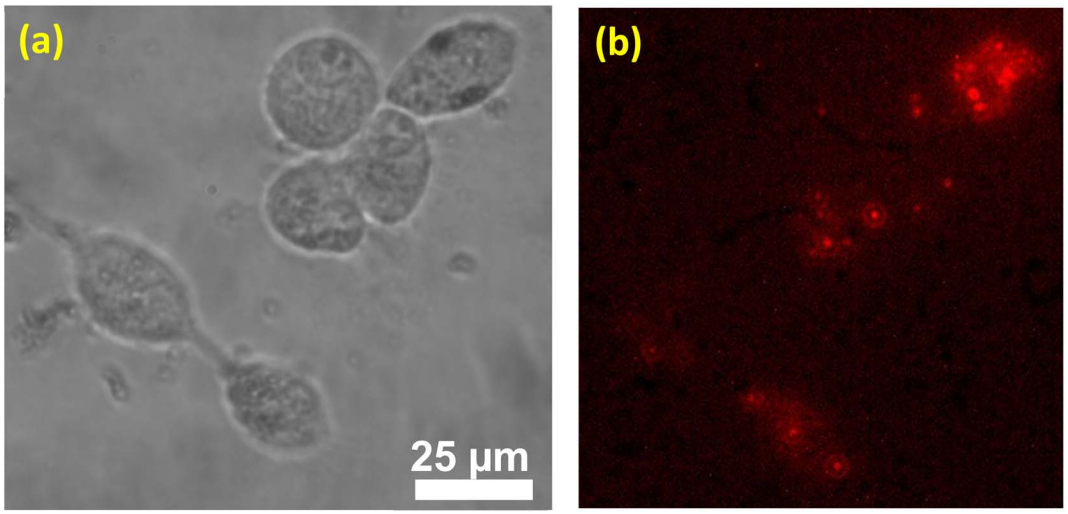

Fig. 14 Fluorescence microscopy images of (a) control sample and (b) U-87 living cells incubated with TGA-Ag_2S nanoparticles.

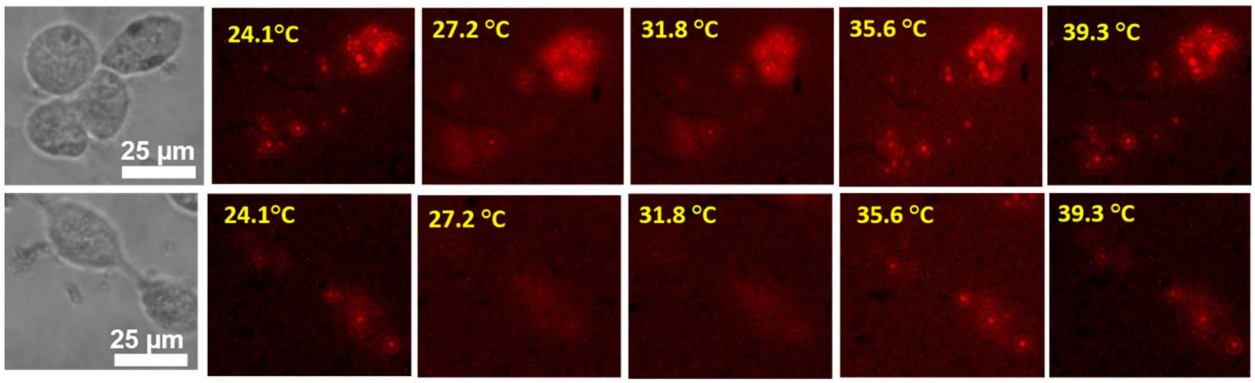

Fig. 15 Fluorescence images of U-87 MG living cells incubated with TGA-Ag_2S nanoparticles and recorded at different temperatures under an excitation wavelength equal to 488 nm.

similarly to the results observed by dispersing Ag_2S nanoparticles in water. Indeed, as indicated in Fig. 16, the decrease was not sufficiently important than that observed with Ag_2S dispersed in water. This may due to the narrower investigated temperature range and the lower laser output power used in presence of living cells. The obtained results demonstrate that these nanoparticles may be used as a suitable tool for both imaging and sensing the temperature inside the living cells. We note also that the aspect of fluoresce coming from the individual cells changes as the temperature increases. This indicates that by using a convenient apparatus for cell imaging, it is possible to map the temperature inside the entire cell which may be a powerful approach to investigate the effects of many factors such pH, drugs and external hazardous species and infections on the dynamic of cellular processes and events that occur in the living cells and to provide information regarding their status. Indeed, all chemical reactions that and biological processes happen may release or absorb heat which results in spatial temperature distribution within the living cell.

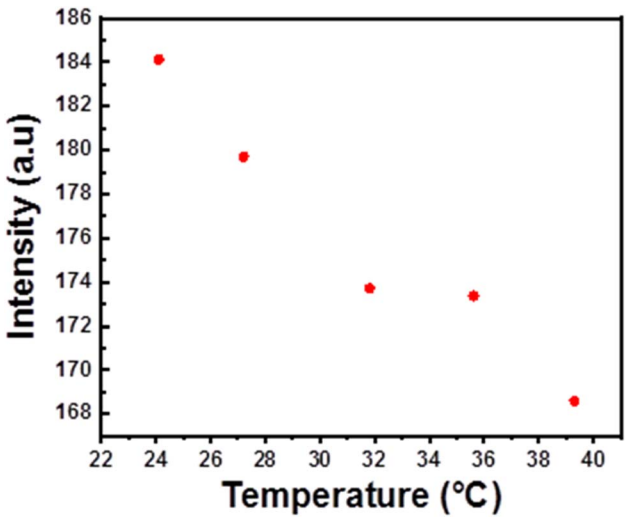

Fig. 16 Evolution with temperature of the PL intensity extracted from Fluorescence images of U-87 MG living cells incubated with TGA-Ag_2S nanoparticles and recorded at different temperatures under an excitation wavelength equal to 488 nm.

4. Conclusion

In summary, we have reported in this work a simple method to synthetize water-soluble TGA-Ag_2S nanoparticles emitting in the NIR biological window. FTIR investigation have showed that TGA thiol molecules are fixed to the surface of these nanoparticles. From TEM images, we have shown that the prepared nanocrystals have nearly spherical shapes whereas some of them form large aggregates. From HRTEM image, we have deduced that Ag_2S nanoparticles have a monoclinic crystalline phase. We have shown by EDS analysis that these nanoparticles have an Ag/S ratio nearly equal to 2.2, which is slightly higher than the theoretical ratio of corresponding to perfect Ag_2S crystal (Ag/S = 2). From the PL study, we may conclude that the prepared nanoparticles are stable at physiologically relevant conditions (pH, ionic force, temperature) increasing their potential use in biological applications. The cytotoxicity of the as-prepared Ag_2S nanoparticles was evaluated by MTT assay using U-87 human living cells. The obtained results have demonstrated good biocompatibility of these nanoparticles with a viability ratio higher than 80%. Fluorescence imaging has evidenced an effective internalization of these nanoparticles inside the living cells. We have also shown that these nanoparticles were photostable, and may be stored for at least six months in atmospheric environment at 4 °C without losing their emissive properties. Additionally, the reversible thermal quenching of the infrared PL emission and the internalization of these nanoparticles together with their biocompatibility may be exploited to explore the temperature and to investigate the dynamical and chemical processes that happen inside the living cells or the biological medium.

Conflicts of interest

There are no conflicts to declare.

References

1 J. E. Hulla, S. C. Sahu and A. W. Hayes, *Hum. Exp. Toxicol.*, 2015, **34**, 1318–1321, DOI: 10.1177/0960327115603588.
2 N. Joudeh and D. Linke, *J. Nanobiotechnol.*, 2022, **20**, 5, DOI: 10.1186/s12951-022-01477-8.
3 E. Dabirian, A. Hajipour, A. Abouei Mehrizi, C. Karaman, F. Karimi, P. Loke-Show and O. Karaman, *Fuel*, 2023, **331**, 125682, DOI: 10.1016/j.fuel.2022.125682.
4 D. Mittal, G. Kaur, P. Singh, K. Yadav and S. A. Ali, *Front. Nanotechnol.*, 2020, **2**, 38, DOI: 10.3389/fnano.2020.579954.
5 K. E. Hurst, J. M. Luther, C. Ban and S. T. Christensen, Nanomaterials for Energy Applications, in *Metrology and Standardization of Nanotechnology*, ed. E. Mansfield, D. L. Kaiser, D. Fujita and M. Van de Voorde, 2017, ch. 28, DOI: 10.1002/9783527800308.
6 D. Astruc, *Chem. Rev.*, 2020, **120**, 461–463, DOI: 10.1021/acs.chemrev.8b00696.
7 S. Bayda, M. Adeel, T. Tuccinardi, M. Cordani and F. Rizzolio, *Molecules*, 2020, **25**, 12, DOI: 10.3390/molecules25010112.
8 S. C. Baetke, T. Lammers and F. Kiessling, *Brit. J. Radiol.*, 2015, **88**, 20150207, DOI: 10.1259/bjr.20150207.
9 S. Sim and K. Wong, *Biomed. Rep.*, 2021, **14**, 9, DOI: 10.3892/br.2021.1418.
10 J. Lan, *Contrast Media Mol. Imaging*, 2022, 3507383, DOI: 10.1155/2022/3507383.
11 P. Wang, N. W. Menzies, E. Lombi, R. Sekine, F. P. Blamey, *et al.*, *Nanotoxicology*, 2015, **9**, 1041–1049, DOI: 10.3109/17435390.2014.999139.
12 G. Chen, F. Tian, Y. Zhang, Y. Zhang, C. Li and Q. Wang, *Adv. Funct. Mater.*, 2014, **24**, 2481–2488, DOI: 10.1002/adfm.201303263.
13 Y. Zhang, G. Hong, Y. Zhang, G. Chen, F. Li, H. Dai and Q. Wang, *ACS Nano*, 2012, **6**, 3695–3702, DOI: 10.1021/nn301218z.
14 A. Ortega-Rodríguez, Y. Shen, I. Zabala Gutierre, *et al.*, *ACS Appl. Mater. Interfaces*, 2020, **12**, 12500–12509, DOI: 10.1021/acsami.9b22827.
15 G. Hong, J. T. Robinson, Y. Zhang, S. Diao, A. L. Antaris, Q. Wang and H. Da, *Angew. Chem., Int. Ed.*, 2012, **51**, 9818–9821, DOI: 10.1002/anie.201206059.
16 S. Chinnathambi and N. Shirahata, *Sci. Technol. Adv. Mater.*, 2019, **20**, 337–355, DOI: 10.1080/14686996.2019.1590731.
17 F. D. Duman, I. Hocaoglu, D. Gulfem, O. D. Gozuacik, A. Kiraza and H. Y. Acar, *Nanoscale*, 2015, **7**, 11352–11362, DOI: 10.1039/c5nr00189g.
18 C. Ding, Y. Huang, Z. Shen and X. Chen, *Adv. Mater.*, 2021, **33**, 29, DOI: 10.1002/adma.202007768.
19 D. Aydemir, M. Hashemkhani, H. Yagci Acar and N. N. Ulusu, *Mol. Biol. Rep.*, 2020, **47**, 4117–4129, DOI: 10.1007/s11033-020-05522-3.
20 T. Kondratenko, O. Ovchinnikov, I. Grevtseva, M. Smirnov, O. Erina and V. Khokhlov, *Materials*, 2020, **13**, 909, DOI: 10.3390/ma13040909.
21 O. V. Ovchinnikov, I. G. Grevtseva, M. S. Smirnov, T. S. Kondratenko, *et al.*, *Opt. Quantum Electron.*, 2020, **52**, DOI: 10.1007/s11082-020-02314-8.
22 W. R. Thompson, M. Cai, M. Ho and J. E. Pemberton, *Langmuir*, 1997, **13**, 2291–2302, DOI: 10.1021/la960795g.
23 O. Ovchinnikov, S. Aslanov, M. Smirnov, A. Perepelitsa, T. Kondratenko, A. Selyukov and I. Grevtseva, *Opt. Mater. Express*, 2021, **11**, 89–104, DOI: 10.1364/OME.411432.
24 A. Pallipurath, Ol. Nicoletti, J. M. Skelton, S. Mahajan, P. A. Midgley and S. R. Elliott, *Ultrason. Sonochem.*, 2014, **21**, 1886–1892, DOI: 10.1016/j.ultsonch.2014.03.014.
25 S. Mourdikoudis, R. M. Pallares and N. K. Thanh, *Nanoscale*, 2018, **10**, 12871–12934, DOI: 10.1039/c8nr02278j.
26 J. Wan, Y. Kim, M. J. Mulvihill and T. K. Tokunaga, *Environ. Toxicol. Chem.*, 2018, **37**, 1301–1308, DOI: 10.1002/etc.4103.
27 M. S. Leon-Velaquez, R. Irizarry and M. E. Castro-Rosario, *J. Phys. Chem. C*, 2010, **114**, 5839–5849, DOI: 10.1021/jp911238a.
28 M. Park, D. Choi, Y. Choi, H. Shin and K. S. Jeong, *ACS Photonics*, 2018, **5**, 1907–1911, DOI: 10.1021/acsphotonics.8b00291.

29 W. J. Mir, A. Swarnkar, R. Sharma, A. Katti, K. V. Adarsh and A. Nag, *J. Phys. Chem. Lett.*, 2015, **6**, 3915–3922, DOI: **10.1021/acs.jpclett.5b01692**.
30 L. Brus, *J. Phys. Chem.*, 1986, **90**(12), 2555–2560, DOI: **10.1021/j100403a003**.
31 S. H. Ehrlich, *J. Imaging Sci. Technol.*, 1993, **37**, 73–91.
32 D. Asik, M. B. Yagci, F. Demir Duman and H. Yagci Acar, *J. Mater. Chem. B*, 2016, **4**, 1941–1950, DOI: **10.1039/C5TB02599K**.
33 T. Muñoz-Ortiz, L. Abiven, R. Marin, J. Hu, D. H. Ortgies, A. Benayas, F. Gazeau, V. Castaing, *et al.*, *Opt. Quantum Electron.*, 2022, 2200100, DOI: **10.1002/ppsc.202200100**.
34 Y. Zhao, C. Riemersma, F. Pietra, R. Koole, C. de Mello Donega and A. Meijerink, *ACS Nano*, 2012, **6**, 9058–9067, DOI: **10.1021/nn303217q**.
35 A. Olkhovets, R. C. Hsu, A. Lipovskii and F. Wise, *Phys. Rev. Lett.*, 1998, **81**, 3539, DOI: **10.1103/PhysRevLett.81.3539**.
36 K. Wei, Z. Xu, R. Chen, X. Zheng, X. Cheng and T. Jiang, *Opt. Lett.*, 2016, **41**, 3821–3824, DOI: **10.1364/OL.41.003821**.
37 J. C. van der Bok, D. M. Dekker, M. L. J. Peerlings, B. B. V. Salzmann and A. Meijerink, *J. Phys. Chem. C*, 2020, **124**, 12153–12160, DOI: **10.1021/acs.jpcc.0c03048**.
38 B. T. Diroll, M. S. Kirschner, P. Guo and R. D. Schaller, *Annu. Rev. Phys. Chem.*, 2019, **70**, 353–377, DOI: **10.1146/annurev-physchem-042018-052639**.
39 Q. Liang, *J. Nanomed. Nanosci.*, 2017, **2**, 6, DOI: **10.29011/JNAN-136.100036**.
40 W. J. Mir, A. Swarnkar, R. Sharma, A. Katti, K. V. Adarsh and A. Nag, *J. Phys. Chem. Lett.*, 2015, **19**, 3915–3922, DOI: **10.1021/acs.jpclett.5b01692**.
41 M. Jones, S. S. Lo and G. D. Scholes, *Proc. Natl. Acad. Sci. U.S.A.*, 2009, **106**, 3011–3016, DOI: **10.1073/pnas.0809316106**.
42 X. Cai, J. E. Martin, L. E. Shea-Rohwer, K. Gong and D. F. Kelley, *J. Phys. Chem. C*, 2013, **117**(15), 7902–7913, DOI: **10.1021/jp400688g**.
43 D. R. Jung, J. Kim and B. Park, *Appl. Phys. Lett.*, 2010, **96**(4), 211908, DOI: **10.1063/1.3431267**.
44 Yu Zhang, Mi Lan, P.-N. Wang, J. Ma and Ji-Y. Chen, *J. Lumin.*, 2008, **128**, 1948–1951, DOI: **10.1016/j.jlumin.2008.06.004**.
45 T. S. Ponomaryova, V. V. Olomskaya, A. S. Novikova and I. Yu. Goryacheva, *Izv. Sarat. Univ. Physics*, **23**(3), 238–244, DOI: **10.18500/1817-3020-2023-23-3-238-244**.
46 C. Gota, K. Okabe, T. Funatsu, Y. Harada and S. Uchiyama, *J. Am. Chem. Soc.*, 2009, **131**, 2766–2767, DOI: **10.1021/ja807714j**.
47 F. Tang, C. Wang, J. Wang, X. Wang and L. Li, *ACS Appl. Mater. Interfaces*, 2014, **6**, 18337–18343, DOI: **10.1021/am505776a**.
48 Y. Chen, Y. Xue, Q. Mao, L. Pei, *et al.*, *J. Mater. Chem. C*, 2023, **11**, 19974–19983, DOI: **10.1039/D3TC01780J**.
49 Y. Shen, H. D. A. Santo, *et al.*, *Adv. Funct. Mater.*, 2020, 2002730, DOI: **10.1002/adfm.202002730**.
50 J. Lifante, Y. Shen, I. Z. Gutierrez, *et al.*, *Adv. Sci.*, 2021, 11, DOI: **10.1002/advs.202003838**.
51 K. Nigoghossian, B. Bouvet, *et al.*, *Nanomaterials*, 2022, **12**, 20, DOI: **10.3390/nano12183109**.
52 M. Suta, Z. Antic, V. Dorđevic, S. Kuzman, M. D. Dramicanin and A. Meijerink, *Nanomaterials*, 2020, **10**, 20, DOI: **10.3390/nano10030543**.